

Thermal-mechanical-electrical energy conversion system based on Curie effect and soft-contact rotary triboelectric nanogenerator

Xiaole Cao^{1,2}, Xuelian Wei^{1,2}, Ruonan Li¹, ZhongLin Wang^{1,2,3} (✉), and Zhiyi Wu^{1,2,4} (✉)

¹ Beijing Institute of Nanoenergy and Nanosystems, Chinese Academy of Sciences, Beijing 101400, China

² School of Nanoscience and Technology, University of Chinese Academy of Sciences, Beijing 100049, China

³ School of Materials Science and Engineering, Georgia Institute of Technology, Atlanta, GA 30332, USA

⁴ CUSTech Institute of Technology, Wenzhou 325024, China

© Tsinghua University Press 2022

Received: 30 July 2022 / Revised: 6 September 2022 / Accepted: 14 September 2022

ABSTRACT

Untapped thermal energy, especially low-grade heat below 373 K from various sources, namely ambient, industries residual, and non-concentrated solar energy, is abundant and widely accessible. Despite that, there are huge constraints to recycle this valuable low-grade heat using the existing technologies due to the variability of thermal energy output and the small temperature difference between the heat source and environment. Here, a thermal-mechanical-electrical energy conversion (TMEc) system based on the Curie effect and the soft-contact rotary triboelectric nanogenerator (TENG) is developed to recycle thermal energy in the mid-low temperature range. According to the phase transition mechanism between ferromagnetic and paramagnetic, disk-shaped ferromagnetic materials can realize stable rotation under external magnetic and thermal fields, thus activating the operation of TENGs and realizing the conversion of thermal energy and electrical energy. During the steady rotation process, an open-circuit voltage (V_{OC}) of 173 V and a short-circuit current (I_{SC}) of 1.32 μ A are measured. We finally obtained a maximum power of 4.45 mW in the actual working conditions, and it successfully charged different capacitors. This work provides a new method for mid-low temperature energy harvesting and thermal energy transformation and broadens the application of TENG in the field of thermal energy recovery.

KEYWORDS

low-grade thermal energy, Curie effect, triboelectric nanogenerator, thermal energy harvesting

1 Introduction

The improvement of energy efficiency has become an important issue related to world industrialization and economic development. In the field of heat engines, from the era of the steam engine to the so-called supercritical steam turbine, the temperature of the steam is expected to be as high as possible. Based on Carnot's law, the higher the temperature of the working material, the higher the efficiency of the heat engine [1, 2]. However, heat below 373 K, such as waste thermal energy in food processing, crude oil processing, and organic chemical processes, belongs to low-grade thermal or "garbage thermal", which is often discarded [3–5]. Traditional thermoelectric power generation technology is still challenging in collecting and utilizing low-grade thermal energy due to the variability of thermal energy output and the small temperature difference between the heat source and environment [6, 7]. A large amount of low-grade thermal energy is discharged into the environment, resulting in serious energy waste and thermal pollution to the surrounding environment [8]. Therefore, dexterous utilization and versatile conversion of the waste thermal energy is now considered as the sustenance of the decarbonized and sustainable ecosystem [9–11]. Recently, novel systems and mechanisms have emerged to attempt to extract and recycle this ubiquitous waste thermal energy, and one approach is to convert thermal energy into mechanical work, such as thermo-

osmotic energy conversion [12–14]. Another route is to harvest thermal energy for electricity output, including thermoelectric [15, 16], pyroelectric transducers [17–19], and water-evaporation-induced generators [20–24]. These works generally suffer from low output performance, which limits their application. Therefore, autonomous and continuous extraction and utilization of the low-grade thermal energy from a constant ambient environment is still an enormous challenge [25, 26].

Based on the coupling effect of triboelectricity and electrostatic induction, triboelectric nanogenerators (TENGs) can efficiently convert ambient mechanical energy into electrical energy, especially for low-frequency, irregular, and widely distributed vibrational energy [27–30]. The TENG has tremendous advantages of low cost, lightweight, simple fabrication process, and high flexibility compared to the traditional energy harvesting methods [31–34]. And it has been reported to harvest sustainable energy such as wind energy, ocean wave energy, thermal energy, biomechanical energy, and even droplet energy [35–39]. Some hybrid energy harvesting units have been reported successful to harvest thermal energy and convert it into electricity [40–45]. Lee et al. recently confirmed the potential of the TENG based on the shape memory alloy-wire for low-grade heat harvesting and obtained an open-circuit voltage (V_{OC}) of 24.5 V [40]. Subsequently, Li et al. proposed a hybrid triboelectric-

Address correspondence to ZhongLin Wang, zlwang@gatech.edu; Zhiyi Wu, wuzhiyi@binn.cas.cn

electromagnetic nanogenerator based on the shape memory alloy to further improve the output performance [41]. However, shape memory alloys are relatively expensive and prone to fracture, which limits their further application in the field of energy harvesting. On the other hand, there are problems such as impedance mismatch and working temperature mismatch due to the different working principles of the hybrid generators. Our group has proposed a thermal-mechanical-electrical energy conversion (TMEc) system based on the Curie effect, mainly using the contact separation mode of TENG, and obtained a V_{OC} of 218 V [42]. But since the ferromagnetic phase and paramagnetic phase switching process takes a period of time, the energy harvesting system is a discontinuous process, which results in a discontinuous output and limits its further application.

Here, we further developed a TMEc system based on the Curie effect and soft-contact rotary triboelectric nanogenerator (SCR-TENG) to recycle thermal energy in the mid-low temperature range. This system can be dissected into two small procedures of energy transformation: thermal-mechanical and mechanical-electrical. The working principle of rotation of the ferromagnetic material is studied and analyzed with infrared detection, finite element simulation, and force analysis. In order to realize the harvesting and utilization of low-grade thermal energy, the thermo-mechanical energy conversion process based on the Curie effect and the mechanical-electrical energy process based on TENG were designed and optimized, respectively, and finally obtained an open-circuit voltage (V_{OC}) of 174 V, short-circuit current (I_{SC}) of 1.32 μ A, and transfer charge (Q_{SC}) of 103.8 nC. The framed rabbit fur on the surface of the FEP film is used to generate high-density charges and improve the durability of TENG. After 86,400 operating cycles, the I_{SC} of TENG has no obvious attenuation. The TMEc system generates a considerable electrical output, charges different capacitors by the stable rotation, and lights up the arrow lined with light-emitting diodes (LEDs) to indicate the direction.

2 Results and discussion

2.1 Design of TMEc system

Ferromagnetic materials have strong magnetism after being magnetized [46]. With the increase of temperature, the enhancement of the thermal motion of the metal lattice will affect the ordered arrangement of the magnetic moment in the magnetic domain. When the temperature is high enough to destroy the ordered arrangement of the magnetic moment, the magnetic domain is disintegrated, the average magnetic moment becomes zero, and the magnetism of the ferromagnetic substance disappears and becomes paramagnetic. The corresponding temperature at this time is called the Curie point, also known as the Curie temperature (T_C) or the magnetic transition point, and is the critical point at which ferromagnetic substances are transformed into paramagnetic substances. Therefore, under the action of the external magnetic field, the ferromagnetic material realizes movement in the process of switching between hot and cold zones, thereby realizing the conversion of thermal energy to mechanical energy. TENG, as an efficient energy conversion device, can convert mechanical energy into electrical energy based on contact electrification and electrostatic induction. Therefore, via coupling the Curie effect and TENG, it is expected to realize the conversion from thermal energy to mechanical energy and then to electrical energy. The TMEc system is constructed to demonstrate the feasibility of the above principle, as illustrated in Fig. 1(a). The TMEc system consists of a rotor (a nickel steel welded workpiece, a fur disk) and a stator (printed circuit board (PCB) disk with electrodes). The nickel ring is used as the

ferromagnetic material, which has a lower T_C and low cost (Table S1 in the Electronic Supplementary Material (ESM)), and the circular magnet provides the magnetic field. The freestanding mode TENG completes the conversion from mechanical energy into electrical energy. The rotor and the central shaft are connected with bearings, and three aluminum rods are used to connect the nickel steel welding and the fur disk to realize power transmission. The specific structural assembly is introduced in Fig. S1 in the ESM, and the optical photograph of the TMEc system is shown in Fig. 1(b).

The working mechanism of TMEc system can be divided into three parts: thermomagnetic interaction part, mechanical motion generation part, and TENG power generation part, and two processes of energy conversion including thermo-mechanical and mechanical-electrical. The force analysis of the nickel ring at different temperatures is used to explain the whole rotation process, as shown in Fig. 1(c). The unheated nickel ring exhibits a ferromagnetic phase and can be attracted by the magnet. At this moment, the magnetic domains (black arrows indicate the magnetic domain direction) are ordered along the direction of the magnetic field (the blue dotted line indicates the magnetic induction line). The nickel ring is divided into upper and lower parts by the central axis of the magnet, which are subjected to two directions of the attraction F_2 and F_1 , respectively, and are kept stable under the fixing of the central axis. When the nickel ring is heated with an alcohol lamp, the magnetic domains in the heated area rotate and become disordered due to the enhanced thermal motion of the metal lattice, while the magnetic domains in other areas remain ordered. As a result, the heated area becomes paramagnetic and the magnetic induction lines become smooth. Figure 1(c), (ii) shows the force analysis of the nickel ring under heating. Similarly, the upper and lower parts are subjected to the attraction F_2' and F_1' , respectively. At this moment, due to the conversion of ferromagnetic phase and paramagnetic phase, F_1' is significantly reduced compared to F_1 , and the degree of reduction is greater than that of F_2' , thereby generating a tangential force F along the nickel ring clockwise, and the nickel ring rotates clockwise by a certain angle. With the switching of the ferromagnetic and paramagnetic phases in the new heating area, a new force F is formed, which continues to drive the nickel ring to rotate. As this process progresses, thermomagnetic interaction enables the conversion of thermal energy to mechanical energy (Movie ESM1). Furthermore, the conversion of mechanical to electrical energy is realized via a freestanding mode TENG, as shown in Fig. 1(d).

2.2 Thermo-mechanical energy conversion

To better explain the principle of the Curie effect, the ferromagnetism and paramagnetism transitions of the magnet at different temperatures are simulated by finite element simulation. Figure 2(a) shows the simulation results of magnetic field distribution and temperature distribution at 298 K (Fig. 2(a), (i) and (ii)) and 600 K (Fig. 2(a), (iii) and (iv)) by COMSOL, and only a partial area of the nickel ring is drawn. In 298 K, the nickel ring is ferromagnetic and the magnetic induction line passing through the nickel ring is in a bent state (Fig. 2(a), (i)). As the temperature increases, the magnetic domains are disintegrated, the average magnetic moment becomes zero, and the magnetism of ferromagnetic substances disappears into paramagnetic substances. The magnetic induction line passed the nickel ring becomes smooth.

The rotation speed of the nickel ring is an important evaluation parameter for the thermal energy-mechanical energy process. The influence factors, such as the magnet placement angle, position, and nickel ring radius, to the rotation speed are explored. Here, we

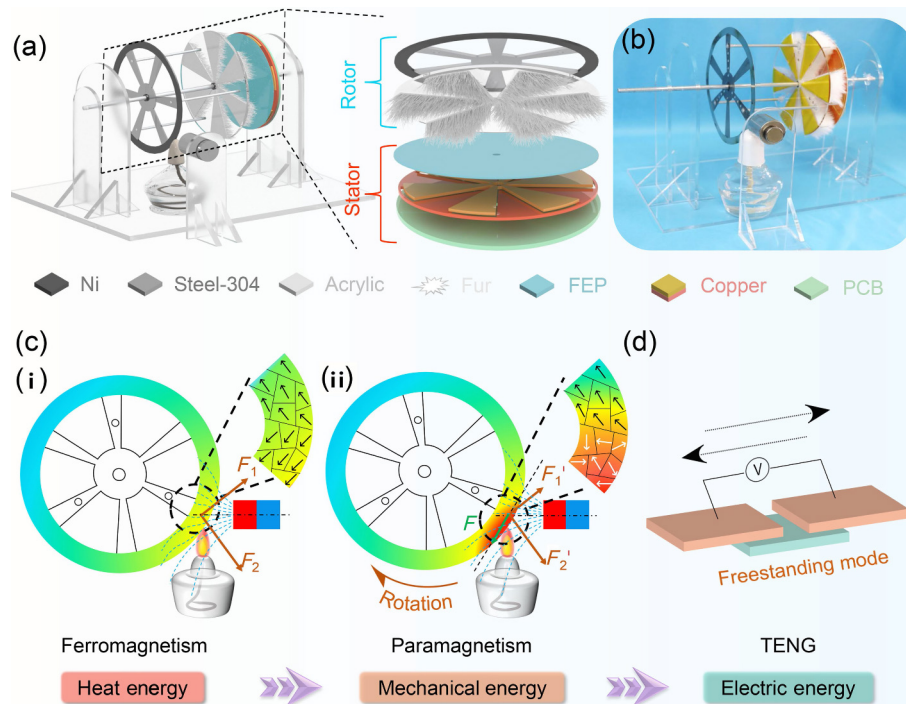


Figure 1 Schematic illustration and working mechanism of the TMEc system based on Curie effect and soft contact rotary TENG. (a) Structural schematic of TMEc system and schematic diagram of the TENG composed of rotators (welded workpiece of nickel and steel, fur disk) and stators (PCB disk with the electrode). (b) Optical photograph of the TMEc system. (c) Schematic diagram of the working principle of TMEc system. Force analysis of nickel ring at different temperatures in the process of converting thermal energy to mechanical energy. The enlarged part shows the effect of temperature on the magnetization direction of magnetic materials, the blue line is the magnetic induction line, and the arrow represents the magnetization direction. (d) Mechanical energy is transferred into electrical energy by freestanding triboelectric-layer mode.

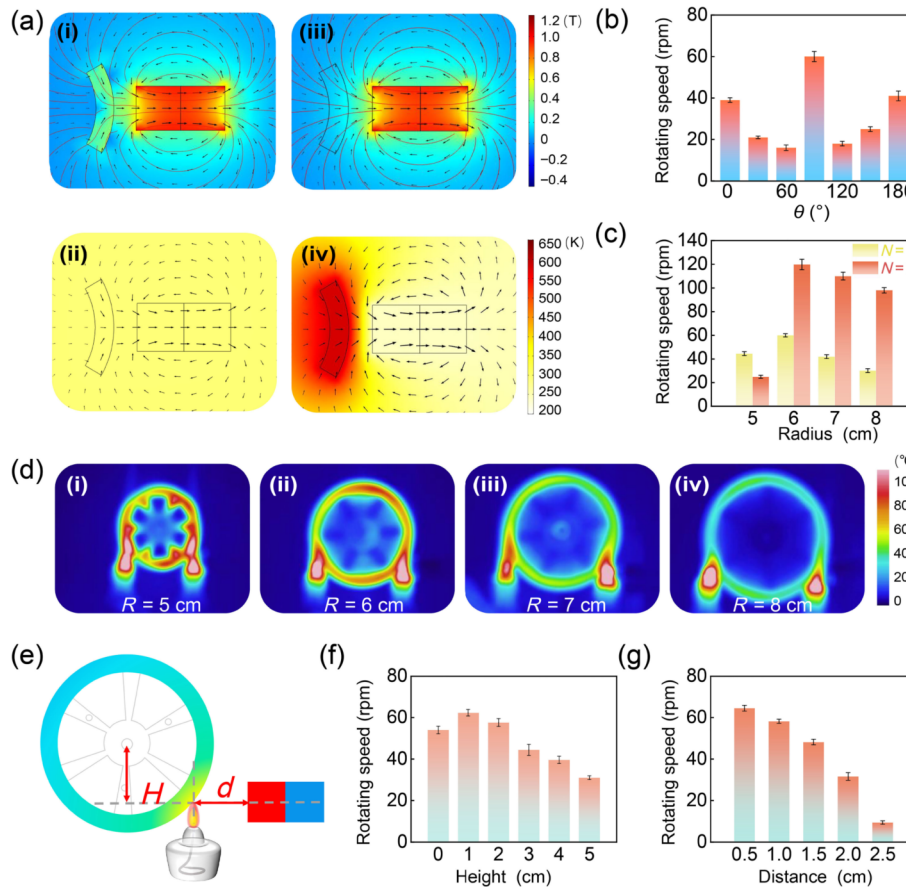


Figure 2 The principle and structure optimization of thermo-mechanical energy conversion. (a) COMSOL simulation of Curie effect, simulation results of magnetic field distribution and temperature distribution at ((i) and (ii)) 298 and ((iii) and (iv)) 600 K. (b) Influence of magnet angle on rotational speed. (c) Influence of Ni disk radius and number of heating sources on its rotational speed. (d) Thermal images of nickel disks with different radii under stable rotation. (e) The schematic diagram of the position of the magnet, including the height difference between the magnet and the central axis, and the distance D between the magnet and the hot spot of the nickel plate. The influence of the position of the magnet on the rotational speed ($R = 8$ cm), including the (f) height (H) and (g) D .

chose N42 magnets (30 mm × 20 mm) for follow-up experiments according to the experimental needs [42]. The direction of the magnetic field determines the force direction of the nickel ring, so the different placement angles of the magnets affect the magnitude of the force on the nickel ring and thus the rotation speed. Figure S2 in the ESM depicts the placement angles of the magnet. When the magnet is placed at an angle of 90°, the nickel ring ($R = 6$ cm) achieves the maximum rotation speed of 62 rpm with one alcohol lamp, as measured in Fig. 2(b). The alternation of the ferromagnetic phase and paramagnetic phase caused by the cyclic switching between hot and cold regions zones is the basis for the stable rotation of the nickel ring. As shown in Fig. 2(c), we investigated the effect of nickel rings of different radii and the number of heat sources on the rotational speed, and Fig. S3 in the ESM shows the photograph of the nickel rings with different radii. The experimental results show that two heating sources can effectively increase the rotation speed of the nickel ring except for nickel rings with a radius of 5 cm. And with the increase of the radius, the rotation speed first increases and then slowly decreases. The main reason can be explained by the cooling/heating cycle. Nickel rings with different radii affect the cooling time, for the small-radius nickel ring (e.g., $R = 5$ cm), has shorter cooling times due to shorter movement paths in the heated area, the entire nickel ring is mainly in the paramagnetic phase after a while. The resultant force F of the upper and lower parts gradually decreases or even disappears, causing the nickel ring to stop rotating. Therefore, one heating source is more beneficial to the nickel ring with a radius of 5 cm. At this time, the nickel ring can rotate stably, and Fig. S4(a) in the ESM shows the infrared thermal image of its stable rotation under one heat source. Conversely, as the radius increases, take the nickel ring with an 8 cm radius as an example. During the rotation process, the heated area of the nickel ring gradually cooled down and recovered the ferromagnetic phase, while the new heating area did not complete the conversion from the ferromagnetic phase to the paramagnetic phase, resulting in discontinuous rotation (Fig. S4(b) in the ESM). Therefore, the rotation speed increases first and then decreases with the increase of the radius. Figure 2(d) and Movie ESM2 show the thermal images of the rotation process of nickel rings with different radii under the condition of two heating sources. The temperature region of the nickel ring with a small radius is significantly higher than that of the nickel ring with a large radius, which also confirms our conjecture. In addition, during the experiment, it was found that the nickel ring exists the phenomenon of unstable rotation (that is, alternating clockwise and counterclockwise rotation). The force analysis was carried out as shown in Fig. S5 in the ESM. The main reason is that when the heated area of state 1 moves to the position of state 2, a counterclockwise tangential force F is generated, which makes the nickel ring rotate counterclockwise. The results of infrared thermal imaging also proved this inference (Fig. S5(c) in the ESM and Movie ESM3). Therefore, as the linear speed is large enough, when the nickel ring can smoothly cross the position generated by the reverse force F , it will maintain a stable rotation state. The essential reason for the unstable rotation is the uneven and discontinuous heating, so in addition to adding a heating source, preheating can still be carried out by manually assisting the rotation to bring the heating and cooling rate of the nickel disk to a stable state.

Although the nickel ring with a radius of 6 cm has the highest rotational speed, the nickel disk area influences the TENG's output performance. Large area TENG can achieve better output performance and the nickel ring with a radius of 8 cm is selected for subsequent experiments. The nickel ring is welded with stainless steel hub and assembled with the acrylic substrate with fur by three aluminum rods. Due to the load of the fur disk, it will

inevitably affect the speed of the nickel ring. According to the moment of inertia equation

$$I = mr^2 \quad (1)$$

for a particle, m is the mass, and r is the vertical distance between the particle and the axis of rotation. The load of the fur disk increases the mass m , the moment of inertia becomes larger, the torque becomes smaller, so that the rotational speed decreases.

As mentioned in the previous section, the resultant force F is formed by the force generated by the change of the ferromagnetic phase and paramagnetic phase state of the upper and lower parts of the nickel ring. The magnitude and direction of the force are determined by the direction of the magnetic field, so obtaining the best magnet position helps to improve the conversion efficiency of thermo-mechanical energy. As shown in Fig. 2(e), the position of the magnet has two parameters, D (the distance between the magnet and the center of the heat source) and H (the vertical distance between the magnet's central axis and the center of the circle). The results show that with the increase of H , the rotational speed first increases from 54 to 62 rpm and then decreases to 31 rpm (Fig. 2(f)). When $H = 0$, the central axis of the magnet is coaxial with the center of the ring. At this time, since the heat source is an alcohol lamp, the heated area and the central axis of the magnet cannot be on the same horizontal line, so the rotation speed is smaller than that when $H = 1$ cm. As shown in Fig. 2(g), the rotational speed decreases with the increase of distance D , mainly due to the weakening of the magnetic field as D increases, resulting in a smaller resultant force, F .

2.3 Mechanical-electrical energy conversion

As an emerging energy converting technology, TENG can convert mechanical stimuli into electrical energy owing to the triboelectrification and electrostatic induction, thus enabling the construction of self-powered sensors and systems. Considering that the main conversion form of thermomechanical energy conversion is rotation, the turntable structure of TENG with the freestanding mode is selected. Apart from the flexibility and portability of the TENG, a wide selection of materials has been demonstrated. Almost any materials with different electron affinities, sometimes even the same material, can be used to design functional triboelectrification layers. Different triboelectric dielectrics with different operating modes are compared in Fig. S6 in the ESM. In the conductor–dielectric mode, the conductor, such as copper and aluminum, must act as both the triboelectric dielectric and the charge transfer electrode. In the positive dielectric–negative dielectric mode, metal or metal oxide shall be only used as the electrode. In this case, there is a large frictional resistance in the direct contact of the friction pair, which will cause severe material wear during the relative movement [47, 48]. Two soft-contact dielectric layers (soft-contact polytetrafluoroethylene (sPTFE), rabbit fur) are introduced to solve the above problem. The introduction of a soft-contact dielectric layer to separate the stator and rotor not only reduces the frictional resistance of the TENG during operation, protects the surface of the charged dielectric layer, and prolongs the device life, but also greatly improves the output power density of the TENG. Among them, the peak-to-peak V_{OC} , Q_{SC} and I_{SC} of the TENG made of rabbit fur and fluorinated ethylene propylene (FEP) reach a higher value, about 1.24 kV, 259 nC, and 1.80 μ A, respectively. The structure schematic of SCR-TENG is shown in Fig. 3(a), which consists of fan-shaped fur brushes (positive triboelectric dielectric) and FEP films (negative triboelectric dielectric) based on the freestanding mode.

The working process of the SCR-TENG is based on the coupling of triboelectrification and electrostatic induction. During

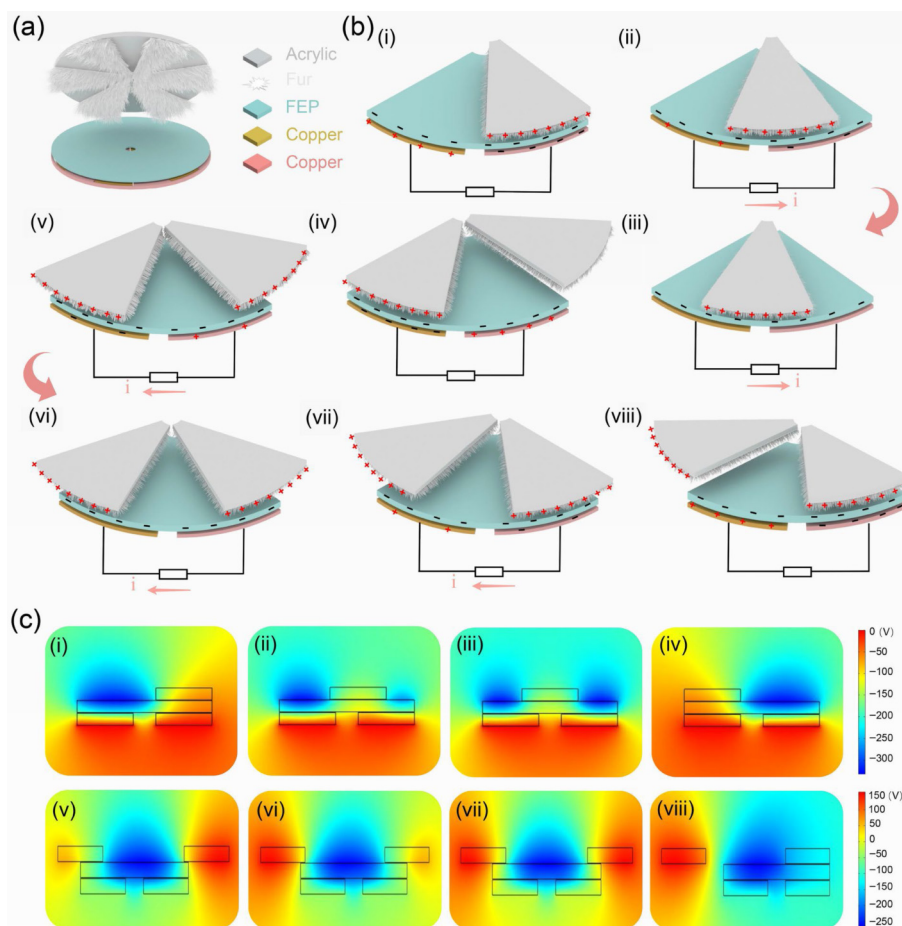


Figure 3 Schematic diagram showing the working principle of the SCR-TENG. (a) Schematic diagram of the soft-contact rotational TENG. (b) Schematic diagram of the working principle of the SCR-TENG for electrostatic induction in the charge-saturated stage. (c) COMSOL simulation results of SCR-TENG corresponding to the rotating state.

the operation process triggered by external mechanical, the FEP films and the fan-shaped fur brushes are in good contact. Electron transfer occurs on the surface through sliding friction, resulting in positive charge on the fur surface and negative charge on the FEP surface. The negative charges on the FEP surface gradually accumulated and reached saturation after several cycles. Owing to the charge conservation, the saturated tribo-charge amounts on the fur sectors and FEP films are equivalent, but the charge density on the FEP is half of that on the fur brushes. Figure 3(b) shows a typical working cycle of the freestanding TENG, only one basic unit of signal generation is introduced to clarify the working mechanism. The state (i), where the fur brush is placed precisely above the right electrode, is taken as the initial condition. Due to electrostatic induction, appropriate negative free charges are induced on the right electrode to balance the excessive positive polarization above it. When the fur sector is rotated clockwise relative to the bottom electrode (states (ii) and (iii)), the positive polarization intensity on the right electrode decreases while the positive polarization intensity on the left electrode gradually increases. The free electrons are redistributed by flowing from the right electrode to the left electrode through the external circuit. The induced current direction from the left to the right electrode is maintained until the FEP gets matched with the right electrode (state (iv)). When the fan-shaped brush rotates further and completely passes through the left electrode (states (vi)–(viii)), the electrons flow backward to the right electrode, generating a reversed current pulse through the external resistance. During the stable rotation, the next fan-shaped fur region continues to repeat this cycle, resulting in the continuous alternating current (AC) output of the SCR-TENG. As shown in Fig. 3(c), COMSOL

carries out corresponding simulations of the potential distribution under the entire rotation process, to observe the power generation process.

2.4 Optimization of SCR-TENG output performance

To optimize the output performance of the SCR-TENG, some factors such as rotational speed, disk radius, contact degree, and interdigital electrode pairing are investigated. A commercial rotating electrical machine measurement system is used for testing. The length of the fur is approximately 20 mm, which can be spread out along the growth direction, and it is directly pasted on the acrylic disk.

The effect of rotational speed on the electrical output performance of the SCR-TENG is firstly investigated, as illustrated in Fig. 4(a) and Fig. S7 in the ESM. Considering the actual rotational speed of the thermomechanical energy conversion process, the output performance under 10–50 rpm is explored. The results show that as the rotational speed increases from 10 to 50 rpm, the V_{OC} and the Q_{SC} are almost stable at 1.7 kV and 320 nC, respectively, and the I_{SC} increases from 0.25 to 1.82 μ A. According to the mechanism of TENG, in the process of triboelectric electrification, the charge amount becomes stable after reaching saturation, regardless of the rotation speed. As for the I_{SC} , referring to Eq. (2), the time course of charge transfer decreases, and the I_{SC} gradually increases

$$I = dQ/dt \quad (2)$$

In addition, the effect of different radii on the output performance of the SCR-TENG is shown in Fig. 4(b) and Fig. S8 in the ESM. The contact area becomes larger as the radius

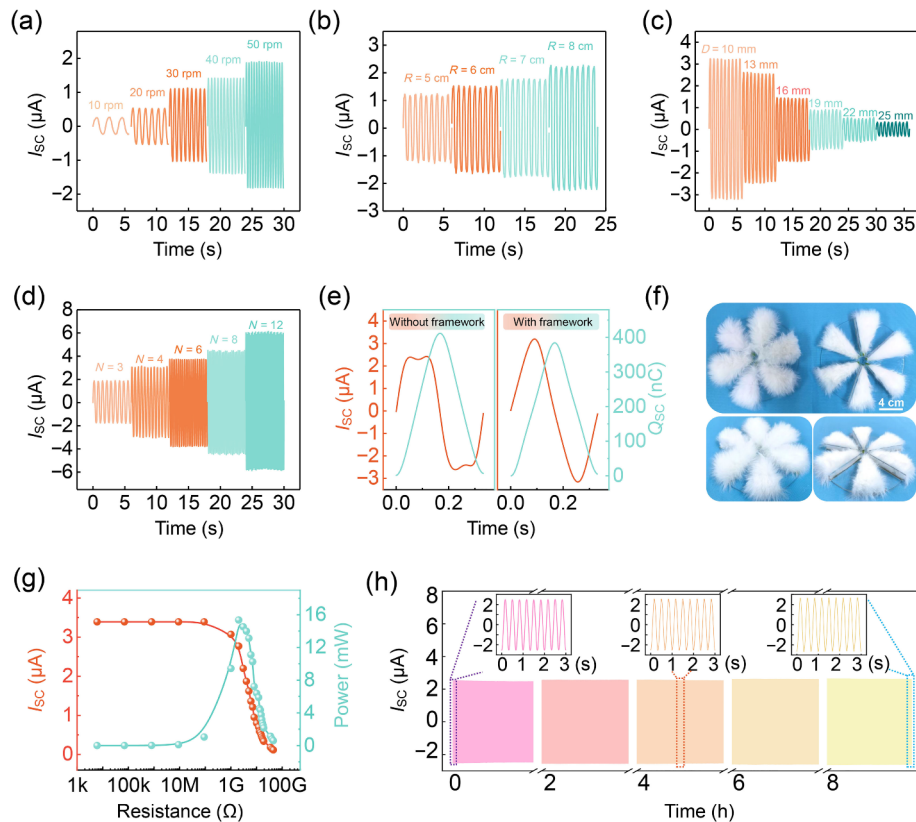


Figure 4 Structural design and optimization of SCR-TEG. (a) The short current (I_{sc}) waveforms at different speeds under the test conditions of rotating electrical machines ($R = 5$ cm, $D = 13$ mm, $N = 3$). (b) Influence of the radius of fur disk on I_{sc} of SCR-TEG ($r = 30$ rpm, $D = 13$ mm, $N = 3$). (c) I_{sc} waveforms of the SCR-TEG with the different internal gaps between acrylic and FEP ($r = 30$ rpm, $N = 3$, $R = 8$ cm). (d) I_{sc} waveforms of the SCR-TEG at the different numbers of interdigitated electrode pairs ($r = 30$ rpm, $R = 8$ cm). (e) Half-periodic pulse wave of the SCR-TEG using the rotors without and with brush framework. (f) Photographs show the rotors with fur brushes without and with the framework. The scale bar is 4 cm. (g) Instantaneous peak current and power-resistance relationship profiles for the SCR-TEG under the selected structural conditions (30 rpm, $R = 8$ cm, $D = 13$ mm, $N = 6$). (h) Cyclic stability test of SCR-TEG under selected structural conditions, the inset is the I_{sc} waveform in the early, middle, and end stages.

increases, and the I_{sc} , V_{oc} , and Q_{sc} gradually increase. Combined with the nickel stainless steel weldment of radius eight selected in the previous section, a fur disk of 8 cm radius is finally chosen for higher output performance.

Besides rotational speed and fur disk radius, the gap D (Fig. S9(a) in the ESM) between the rotor (the acrylic disk with fur adhered) and the FEP disk, which determines the degree of contact, is another crucial factor affecting the output performance of TENG. As the distance decreases from 25 to 10 mm, the I_{sc} gradually increases from 0.32 to 3.24 μA , and the charge increases from 26.2 to 415 nC (Fig. 4(c) and Fig. S9(b) in the ESM). The output performance can be improved by changing the distance or fur length to obtain a good contact state, but at the same time, it should be considered that a good contact state will lead to excessive frictional resistance, so the distance should be changed according to the actual driving force. The influence of the unit of interdigitated electrodes on the triboelectric properties has been tested. As illustrated in Fig. 4(d) and Fig. S10 in the ESM, the Q_{sc} of 3 units is up to 362 nC, and the I_{sc} of 12 units is up to 6.01 μA . With the multiplication of units, the effective contact area decreases, gradually minimizing the V_{oc} and Q_{sc} . Conversely, the time course of charge transfer decreases, and the I_{sc} gradually increases. In order to further optimize the structure of the SCR-TEG, the fur is fixed with an acrylic framework, and the output performance of the two is compared. Magnified views of the I_{sc} and Q_{sc} pulse peaks of the rotor disk with or without frame are shown in Fig. 4(e). The results show that the waveform of the transferred charge is basically the same, but the current is completely different. The peak value of the short-circuit current of the rotor disk with a fixed frame is a sharp peak, and the peak

value of the current without a frame is a flat peak. Moreover, the I_{sc} of the TENG with a fixed frame is higher than that without a frame. The time-integrated value of the current of the rotor disk without the frame is larger than that of the rotor disk with the frame, i.e., the transferred charge is larger. Optical photographs of the framed and unframed rotor disks are shown in Fig. 4(f). The fur of the rotor disk without a fixed frame is scattered and the contact area with the FEP is larger, resulting in a higher transferred charge amount, while the fur with a frame remains upright with clear boundaries of the different sector meshes and no overlapping areas. After considering these factors, we selected the fur fixed with a framework in the following experiments.

Through the exploration of the influence factors of the rotational speed, the radius R of the fur disk, the gap D , the number of interdigital electrode pairs, and rotor disk with or without a frame, the optimal structure of the SCR-TEG was determined. The improved and optimized structure ($R = 8$ cm, $D = 13$ mm, $N = 6$) is tested at 30 rpm, and finally obtains an I_{sc} of 3.23 μA and a Q_{sc} of 389 nC. The electrical outputs when loading a resistor are also characterized, and the peak current-resistance and peak power-resistance relationships are depicted in Fig. 4(g). The instantaneous output power is calculated by

$$P = I_t^2 R \quad (3)$$

where R is the loaded resistance and I_t is the instantaneous current across the resistance. As shown in Fig. 4(g), the instantaneous peak power reaches its maximum value of 14.8 mW at the matched resistance of 1.1 G Ω . Figure 4(h) shows the cycle stability of the SCR-TEG in the 8-h working time. For the FEP-rabbit fur combination, the degree of wear on the surface of the FEP film is

greatly reduced because of the soft contact of fur, and there is almost no remarkable decrease in the output performance after 86,400 cycles.

2.5 Electrical output performance and application of the TMEc system

Through the design and optimization of the thermo-mechanical energy conversion process and the mechanical-electrical energy conversion process, we finally constructed a TMEc system and demonstrated its application prospects in recovering thermal energy in the mid-low temperature range. Figure 5(a) and Movie ESM4 show the optical photograph of the testing environment of the TMEc system.

During the experiment, we found that the resistance during the sliding process between the fur and the FEP is far greater than the driving force of the thermo-mechanical conversion process, which leads to unstable rotation. Two solutions have been adopted to solve this problem. On the one hand, the resultant force F of the thermomagnetic interaction part is improved by increasing the number of magnets. The two magnets alternately generate the force on both sides of the nickel ring, which complements each other to increase the rotational speed, and the force analysis is shown in Fig. S11 in the ESM. Figure 5(b) and Movie ESM5 show the output performance of the TMEc system with different numbers of magnets. The results show that the V_{OC} , I_{SC} , and Q_{SC} are increased to 174 V, 1.32 μ A, and 103.8 nC, respectively. On the other hand, the gap between the fur tip to the FEP membrane surface determines the resistance to sliding friction. The resistance can be reduced by narrowing the gap d , but the output performance is inevitably reduced. As shown in Fig. 5(c), when $d = -0.5$ mm, the unstable electrical output is caused by left and right swinging, and when $d = 0$ mm, that is, when the fur is just in contact with the FEP film, there exists a stable output performance. The final obtained output performance is shown in Figs. 5(d) and 5(e), and Fig. S12 in the ESM, the TMEc system has

a V_{OC} of 174 V, an I_{SC} of 1.32 μ A, and a Q_{SC} of 103.8 nC. The peak current–resistance and peak power–resistance relationships are depicted in Fig. 5(f), where the maximum power value was 4.45 mW in the actual working conditions. Figure 5(g) shows the schematic diagram of the equivalent circuit of the TMEc system charging application, and the charging capability of the TMEc system to the capacitor is shown in Fig. 5(h). For a 47 μ F capacitor, it can be charged to ~ 2 V in 190 s in the actual test environment. For the 1.0, 3.3, 4.7, and 10 μ F capacitors, it takes 15, 28, 48, and 91 s to charge to 4 V, respectively. Additionally, we demonstrate the TMEc system to light up multiple LEDs, as shown in Fig. 5(i). 22 LEDs were assembled to form an arrow indicating the right direction (Movie ESM6).

The mechanism of this system can also be applied to different natural scenes as a means of energy conversion to harvest low-grade waste thermal energy from various sources, such as waste thermal energy in food processing, crude oil processing, and organic chemical processes. And the proposed energy conversion system has applicability in a wide operating temperature range. The energy conversion system based on the magnetocaloric effect can be designed by selecting magnetic materials with different Curie points according to the temperature region of the waste thermal energy in the actual scene. It is obvious that the lower electrical output performance is due to the smaller resultant force generated by the magnetocaloric effect, and the high sliding frictional resistance between the fur and the FEP membrane. The number of magnets has been proven to provide a greater driving force. In the future, the output performance can be improved by increasing the number of magnets and the magnetic energy product of the magnets. In addition, the design and packaging of the TMEc system structure are carried out according to the form of waste thermal energy (gaseous and liquid). On the other hand, varieties of hybrid generators have been developed to effectively improve output performance and energy conversion efficiency, so the electromagnetic generator and TENG can be combined to further improve the output performance of the TMEc system.

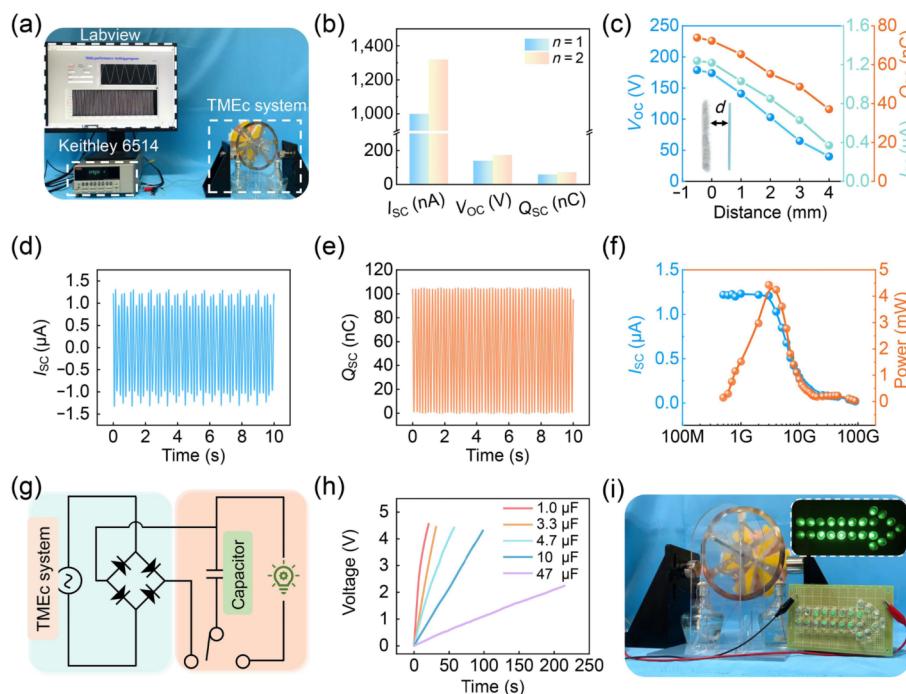


Figure 5 Electrical output performance and application of the TMEc system based on the SCR-TENG. (a) Optical photograph of the testing environment of the TMEc system. (b) Comparison of electrical output performance of SCR-TENG with different numbers of magnets. (c) Attenuation trend of SCR-TENG electrical output performance with the different internal gaps between fur and FEP in TMEc system. (d) I_{SC} curve and (e) Q_{SC} curve of the SCR-TENG of the optimized TMEc system. (f) The instantaneous peak current and power–resistance relationship profiles for the SCR-TENG under the actual working condition. (g) Circuit diagram for driving low-power electronic components with rectifiers and capacitors. (h) Charging curves for different capacitors by the SCR-TENG of the TMEc system. (i) Directly powering LED bulbs for direction indication by the SCR-TENG of the TMEc system.

3 Conclusions

In conclusion, a TMEc system based on the Curie effect and SCR-TENG has been further developed to recover thermal energy in the mid-low temperature range. It shows a prospect for collecting and utilizing various wasted low-grade thermal energy sources such as waste thermal energy in food processing, crude oil processing, and organic chemical processes in the environment. To achieve low-grade thermal energy harvesting, the thermomechanical energy conversion process based on the Curie effect and the mechanical energy conversion electrical energy process based on TENG are designed and optimized. The framed rabbit fur not only generates high-density charges on the surface of the FEP film, but also improves device durability. After 86,400 operating cycles, the short-circuit current has no apparent attenuation. In the verification experiment, the TMEc system can obtain a considerable electrical output and charge different capacitors by the stable rotation. On the other hand, The electrical output can light up arrows assembled from multiple LEDs, to indicate the right direction in special scenes. More improvements and explorations are expected in the future. In all, this work provides a new method for mid-low temperature energy harvesting and thermal energy transformation and widens the application fields of TENGs.

4 Experimental section

4.1 Fabrication of the TMEc system

The TMEc system was assembled from an acrylic frame, nickel stainless steel weldments, SCR-TENG, heat sources, magnets, bearings, and aluminum rods. The acrylic frame was designed and cut by a laser cutting machine (PLS6.75, Universal Laser System). The nickel stainless steel weldments were welded from nickel rings and stainless-steel hubs. The SCR-TENG unit was composed of two parts: a fur disk and an electrode disk. For the fur disk, six sectorized furs with equal-degree radially-arrayed sectors were pasted on the acrylic substrate. The outer diameter and inner diameter of the sectorized furs were 160 and 20 mm, respectively. An acrylic sheet was cut into the desired shape by a laser cutter (PLS6.75) and then double-sided tape (Kapton) was used to attach the fur to the acrylic substrate. Two experimental alcohol lamps served as the heat source. Magnets of N42, bearings, and aluminum rods with different diameters were purchased from the market.

4.2 Characterization and measurement

A hand-held infrared imaging device (Keysight U5857A) was used to monitor and preserve temperature variation. A rotary motor (GFV2G20S) was utilized in the process of SCR-TENG structural design. The magnetic distributions of the magnets with different temperatures were simulated by COMSOL (COMSOL Multiphysics 5.4, Stockholm, Sweden). The short-circuit current, open-circuit voltage, transferred charges, and charging/discharging curves were measured by a programmable electrometer (Keithley Instruments model 6514). A voltage division circuit combined with Keithley 6514 electrometer was used to measure the open-circuit voltage.

Acknowledgements

Research was supported by the National Natural Science Foundation of China (No. 61503051).

Electronic Supplementary Material: Supplementary material

(structural design comparison of TMEc system; placement angle of the magnet; photographs of welded workpieces with different radii; thermal image of the nickel disk with different radii; force analysis of the unstable rotation of the nickel disk; output performance with various triboelectric materials; output electrical performance with different speeds, radii, gaps, and interdigitated electrode pairs; force analysis of the accelerated rotation of two magnet Ni disks; V_{OC} curve of the SCR-TENG of the optimized TMEc system; and Curie point temperature of different ferromagnetic materials. Movie ESM1 shows thermos-mechanical energy conversion; Movie ESM2 shows infrared imaging of thermos-mechanical energy conversion process; Movie ESM3 shows infrared thermal imaging of left-right swing phenomenon; Movie ESM4 shows TMEc system electrical performance testing environment; Movie ESM5 shows the output performance of TMEc system with different numbers of magnets; and Movie ESM6, powering LEDs to indicate the direction by the TMEc system) is available in the online version of this article at <https://doi.org/10.1007/s12274-022-5056-1>.

References

- Chen, L. G.; Sun, F. R.; Wu, C. Influence of heat transfer law on the performance of a Carnot engine. *Appl. Therm. Eng.* **1997**, *17*, 277–282.
- Şahin, B.; Kodal, A.; Yavuz, H. Maximum power density for an endoreversible Carnot heat engine. *Energy* **1996**, *21*, 1219–1225.
- Schierning, G. Bring on the heat. *Nat. Energy* **2018**, *3*, 92–93.
- Shauly, E.; Boo, C.; Lin, S. H.; Elimelech, M. Membrane-based osmotic heat engine with organic solvent for enhanced power generation from low-grade heat. *Environ. Sci. Technol.* **2015**, *49*, 5820–5827.
- Hao, F.; Qiu, P. F.; Tang, Y. S.; Bai, S. Q.; Xing, T.; Chu, H. S.; Zhang, Q. H.; Lu, P.; Zhang, T. S.; Ren, D. D. et al. High efficiency Bi_2Te_3 -based materials and devices for thermoelectric power generation between 100 and 300 °C. *Energy Environ. Sci.* **2016**, *9*, 3120–3127.
- Yu, B. Y.; Duan, J. J.; Cong, H. J.; Xie, W. K.; Liu, R.; Zhuang, X. Y.; Wang, H.; Qi, B.; Xu, M.; Wang, Z. L. et al. Thermosensitive crystallization-boosted liquid thermocells for low-grade heat harvesting. *Science* **2020**, *370*, 342–346.
- Vining, C. B. An inconvenient truth about thermoelectrics. *Nat. Mater.* **2009**, *8*, 83–85.
- Wang, D. X.; Ling, X.; Peng, H.; Liu, L.; Tao, L. L. Efficiency and optimal performance evaluation of organic Rankine cycle for low grade waste heat power generation. *Energy* **2013**, *50*, 343–352.
- Li, T.; Zhang, X.; Lacey, S. D.; Mi, R. Y.; Zhao, X. P.; Jiang, F.; Song, J. W.; Liu, Z. Q.; Chen, G.; Dai, J. Q. et al. Cellulose ionic conductors with high differential thermal voltage for low-grade heat harvesting. *Nat. Mater.* **2019**, *18*, 608–613.
- Garcia, S. I.; Garcia, R. F.; Carril, J. C.; Garcia, D. I. A review of thermodynamic cycles used in low temperature recovery systems over the last two years. *Renew. Sust. Energy Rev.* **2018**, *81*, 760–767.
- Lee, S. W.; Yang, Y.; Lee, H. W.; Ghasemi, H.; Kraemer, D.; Chen, G.; Cui, Y. An electrochemical system for efficiently harvesting low-grade heat energy. *Nat. Commun.* **2014**, *5*, 3942.
- Straub, A. P.; Yip, N. Y.; Lin, S. H.; Lee, J.; Elimelech, M. Harvesting low-grade heat energy using thermo-osmotic vapour transport through nanoporous membranes. *Nat. Energy* **2016**, *1*, 16090.
- Straub, A. P.; Elimelech, M. Energy efficiency and performance limiting effects in thermo-osmotic energy conversion from low-grade heat. *Environ. Sci. Technol.* **2017**, *51*, 12925–12937.
- Shauly, E.; Karanikola, V.; Straub, A. P.; Deshmukh, A.; Zucker, I.; Elimelech, M. Asymmetric membranes for membrane distillation and thermo-osmotic energy conversion. *Desalination* **2019**, *452*, 141–148.
- Bell, L. E. Cooling, heating, generating power, and recovering waste heat with thermoelectric systems. *Science* **2008**, *321*, 1457–1461.

- [16] Hochbaum, A. I.; Chen, R. K.; Delgado, R. D.; Liang, W. J.; Garnett, E. C.; Najarian, M.; Majumdar, A.; Yang, P. D. Enhanced thermoelectric performance of rough silicon nanowires. *Nature* **2008**, *451*, 163–167.
- [17] Lee, J. H.; Ryu, H.; Kim, T. Y.; Kwak, S. S.; Yoon, H. J.; Kim, T. H.; Seung, W.; Kim, S. W. Thermally induced strain-coupled highly stretchable and sensitive pyroelectric nanogenerators. *Adv. Energy Mater.* **2015**, *5*, 1500704.
- [18] Lallart, M.; Yan, L. J.; Miki, H.; Sebald, G.; Diguët, G.; Ohtsuka, M.; Kohl, M. Heusler alloy-based heat engine using pyroelectric conversion for small-scale thermal energy harvesting. *Appl. Energy* **2021**, *288*, 116617.
- [19] Kacem, H.; Dhahri, A.; Sassi, Z.; Seveyrat, L.; Lebrun, L.; Perrin, V.; Dhahri, J. Relaxor characteristics and pyroelectric energy harvesting performance of BaTi_{0.91}Sn_{0.09}O₃ ceramic. *J. Alloys Compd.* **2021**, *872*, 159699.
- [20] Xue, G. B.; Xu, Y.; Ding, T. P.; Li, J.; Yin, J.; Fei, W. W.; Cao, Y. Z.; Yu, J.; Yuan, L. Y.; Gong, L. et al. Water-evaporation-induced electricity with nanostructured carbon materials. *Nat. Nanotechnol.* **2017**, *12*, 317–321.
- [21] Qin, Y. S.; Wang, Y. S.; Sun, X. Y.; Li, Y. J.; Xu, H.; Tan, Y. S.; Li, Y.; Song, T.; Sun, B. Q. Constant electricity generation in nanostructured silicon by evaporation-driven water flow. *Angew. Chem.* **2020**, *132*, 10706–10712.
- [22] Lee, M. S.; Chang, J. W.; Park, K.; Yang, D. R. Energetic and exergetic analyses of a closed-loop pressure retarded membrane distillation (PRMD) for low-grade thermal energy utilization and freshwater production. *Desalination* **2022**, *534*, 115799.
- [23] Ding, T. P.; Liu, K.; Li, J.; Xue, G. B.; Chen, Q.; Huang, L.; Hu, B.; Zhou, J. All-printed porous carbon film for electricity generation from evaporation-driven water flow. *Adv. Funct. Mater.* **2017**, *27*, 1700551.
- [24] Zhu, L. L.; Gao, M. M.; Peh, C.; K. N.; Wang, X. Q.; Ho, G. W. Self-contained monolithic carbon sponges for solar-driven interfacial water evaporation distillation and electricity generation. *Adv. Energy Mater.* **2018**, *8*, 1702149.
- [25] Kishore, R. A.; Priya, S. A review on low-grade thermal energy harvesting: Materials, methods and devices. *Materials* **2018**, *11*, 1433.
- [26] Forman, C.; Muritala, I. K.; Pardemann, R.; Meyer, B. Estimating the global waste heat potential. *Renew. Sust. Energy Rev.* **2016**, *57*, 1568–1579.
- [27] Wang, Z. L. Triboelectric nanogenerator (TENG)—Sparkling an energy and sensor revolution. *Adv. Energy Mater.* **2020**, *10*, 2000137.
- [28] Wang, Z. L. On Maxwell's displacement current for energy and sensors: The origin of nanogenerators. *Mater. Today* **2017**, *20*, 74–82.
- [29] Zhang, T. T.; Wen, Z.; Liu, Y. N.; Zhang, Z. Y.; Xie, Y. L.; Sun, X. H. Hybridized nanogenerators for multifunctional self-powered sensing: Principles, prototypes, and perspectives. *iScience* **2020**, *23*, 101813.
- [30] Xie, L. J.; Zhai, N. N.; Liu, Y. N.; Wen, Z.; Sun, X. H. Hybrid triboelectric nanogenerators: From energy complementation to integration. *Research* **2021**, *2021*, 9143762.
- [31] Liu, W. L.; Wang, Z.; Hu, C. G. Advanced designs for output improvement of triboelectric nanogenerator system. *Mater. Today* **2021**, *45*, 93–119.
- [32] Wang, H. B.; Han, M. D.; Song, Y.; Zhang, H. X. Design, manufacturing and applications of wearable triboelectric nanogenerators. *Nano Energy* **2021**, *81*, 105627.
- [33] Sriphan, S.; Vittayakorn, N. Hybrid piezoelectric-triboelectric nanogenerators for flexible electronics: Recent advances and perspectives. *J. Sci.: Adv. Mater. Devices* **2022**, *7*, 100461.
- [34] Lone, S. A.; Lim, K. C.; Kaswan, K.; Chatterjee, S.; Fan, K. P.; Choi, D.; Lee, S.; Zhang, H. L.; Cheng, J.; Lin, Z. H. Recent advancements for improving the performance of triboelectric nanogenerator devices. *Nano Energy* **2022**, *99*, 107318.
- [35] Jin, X.; Yuan, Z. H.; Shi, Y. P.; Sun, Y. G.; Li, R. N.; Chen, J. H.; Wang, L. F.; Wu, Z. Y.; Wang, Z. L. Triboelectric nanogenerator based on a rotational magnetic ball for harvesting transmission line magnetic energy. *Adv. Funct. Mater.* **2022**, *32*, 2108827.
- [36] Lin, Z. M.; Zhang, B. B.; Zou, H. Y.; Wu, Z. Y.; Guo, H. Y.; Zhang, Y.; Yang, J.; Wang, Z. L. Rationally designed rotation triboelectric nanogenerators with much extended lifetime and durability. *Nano Energy* **2020**, *68*, 104378.
- [37] Wei, X. L.; Zhao, Z. H.; Zhang, C. G.; Yuan, W.; Wu, Z. Y.; Wang, J.; Wang, Z. L. All-weather droplet-based triboelectric nanogenerator for wave energy harvesting. *ACS Nano* **2021**, *15*, 13200–13208.
- [38] Wu, H.; Wang, J. Y.; Wu, Z. Y.; Kang, S. L.; Wei, X. L.; Wang, H. Q.; Luo, H.; Yang, L. J.; Liao, R. J.; Wang, Z. L. Multi-parameter optimized triboelectric nanogenerator based self-powered sensor network for broadband aeolian vibration online-monitoring of transmission lines. *Adv. Energy Mater.* **2022**, *12*, 2103654.
- [39] Yuan, Z. H.; Wei, X. L.; Jin, X.; Sun, Y. G.; Wu, Z. Y.; Wang, Z. L. Magnetic energy harvesting of transmission lines by the swinging triboelectric nanogenerator. *Mater. Today Energy* **2021**, *22*, 100848.
- [40] Lee, D.; Kim, I.; Kim, D. Hybrid tribo-thermoelectric generator for effectively harvesting thermal energy activated by the shape memory alloy. *Nano Energy* **2021**, *82*, 105696.
- [41] Li, R. N.; Wei, X. L.; Shi, Y. P.; Yuan, Z. H.; Wang, B. C.; Xu, J. H.; Wang, L. F.; Wu, Z. Y.; Wang, Z. L. Low-grade heat energy harvesting system based on the shape memory effect and hybrid triboelectric-electromagnetic nanogenerator. *Nano Energy* **2022**, *96*, 107106.
- [42] Wei, X. L.; Zhao, Z. H.; Wang, L. F.; Jin, X.; Yuan, Z. H.; Wu, Z. Y.; Wang, Z. L. Energy conversion system based on Curie effect and triboelectric nanogenerator for low-grade heat energy harvesting. *Nano Energy* **2022**, *91*, 106652.
- [43] Rodrigues, C.; Pires, A.; Gonçalves, I.; Silva, D.; Oliveira, J.; Pereira, A.; Ventura, J. Hybridizing triboelectric and thermomagnetic effects: A novel low-grade thermal energy harvesting technology. *Adv. Funct. Mater.* **2022**, *32*, 2110288.
- [44] Ibrahim, M.; Jiang, J. X.; Wen, Z.; Sun, X. H. Surface engineering for enhanced triboelectric nanogenerator. *Nanoenergy Adv.* **2021**, *1*, 58–80.
- [45] Chen, Y. F.; Gao, Z. Q.; Zhang, F. J.; Wen, Z.; Sun, X. H. Recent progress in self-powered multifunctional e-skin for advanced applications. *Exploration* **2022**, *2*, 20210112.
- [46] Chouhan, L.; Srivastava, S. K. A comprehensive review on recent advancements in d⁰ ferromagnetic oxide materials. *Mater. Sci. Semicond. Process.* **2022**, *147*, 106768.
- [47] Chen, J. H.; Wei, X. L.; Wang, B. C.; Li, R. N.; Sun, Y. G.; Peng, Y. T.; Wu, Z. Y.; Wang, P.; Wang, Z. L. Design optimization of soft-contact freestanding rotary triboelectric nanogenerator for high-output performance. *Adv. Energy Mater.* **2021**, *11*, 2102106.
- [48] Han, J. J.; Feng, Y. W.; Chen, P. F.; Liang, X.; Pang, H.; Jiang, T.; Wang, Z. L. Wind-driven soft-contact rotary triboelectric nanogenerator based on rabbit fur with high performance and durability for smart farming. *Adv. Funct. Mater.* **2022**, *32*, 2108580.